Experimental Demonstration of Elastic-Plastic Wave Propagation in a Discrete Metamaterial

Greg Dorgant[a], **Michael J. Leamy**[b,*]

[a]*George W. Woodruff School of Mechanical Engineering,Georgia Institute of Technology, Atlanta, 30302, GA, USA*
[b]*Department of Mechanical Engineering, University of Vermont, Burlington, 05405, VT, USA*

Abstract

We fabricate a discrete phononic crystal with hysteretic force–deflection behavior analogous to elastic–plastic material response, and then measure its response to harmonic excitation. Slider (or Jenkins) elements are introduced to mimic plastic deformation and a ten-cell phononic crystal is constructed from modular unit cells. Modular construction enables calibration and validation of individual components prior to full integration, which is particularly important for the sliding elements. Subsequent frequency-sweep experiments at both elastic and plastic excitation amplitudes demonstrate pronounced wave attenuation aligned with bandgap frequencies arising from Bragg scattering. The presence of this strong attenuation, even at plastic amplitudes, reveals experimentally that bandgaps can continue to block frequencies into the strongly nonlinear, plastic regime. The fabricated system is expected to facilitate future experimental studies of large-amplitude, elastic–plastic wave propaga-

---

[*] Address all correspondence to this author. E-mail: michael.leamy@uvm.edu

tion.

Keywords: Elastic Metamaterials, Phononic Crystals, Plastic Waves, Wave Propagation, Bandgaps, Jenkins Element

---

1. Introduction

Acoustic and elastic metamaterials, or media geometrically structured to display wave propagation properties atypical of their constitutive material, have received significant attention in the recent past. These materials derive their unique properties from engineered band structures governing the speed and attenuation of wave propagation. Figure 1(b) depicts one such band structure for which the real and imaginary components of the wavenumber are plotted using a single horizontal axis, with the vertical axis indicating the corresponding frequency. The region in which the imaginary wavenumber component is non-zero and positive denotes the bandgap. Frequencies in this region decay evanescently and are thus prohibited from long distance propagation.

Bandgaps can be exploited in frequency filtering [1, 2] and vibration/noise isolation [3, 4, 5, 6, 7], waveguiding [8, 9], and energy harvesting [10, 11, 12]. Metamaterials can also exhibit negative refractive indices [13, 14] and find application in cloaks [15, 16, 17] and signal multiplexing [18, 19]. Additional functionality can be found in metamaterials composed of nonlinear constitutive elements. Amplitude-dependent band structures arising in nonlinear metamaterials yield exceptional wave propagation behavior not present in linear materials. Metamaterials with amplitude-dependent dispersion [20, 21, 22] admit solitary waves [23, 24, 25], break reciprocity [26, 27, 28, 29, 30, 31], and can be used to realize acoustic switches [32, 33], focusing elements [34, 35], and amplitude filters [36, 37]. Although nonlinear elastic (e.g., hyperelastic) constitutive relations are common in the metamaterial literature [21, 38, 39, 40], elastic-plastic constitutive relations have received sparse attention and are warranted when the wave amplitude exceeds the yield limit.

While the first theoretical treatment of plastic wave propagation in solids is commonly attributed [41] to Donnell in 1930 [42], the field began to receive significant attention during the second world war when the general plastic wave propagation theory was developed independently by Taylor [43] in the UK; von Karman and Duwez [44] and White and Griffis [45] in the US; and Rakhmatulin and Shapiro [46, 47, 48] in the USSR. Researchers have since expanded the general theory to include phenomena such as rate-effects [49, 50, 51], thermodynamic considerations [52, 53, 54], and microstructural phenomena [55, 56, 57]. Applications in this field have traditionally focused on dynamic stress-strain curves [58, 43, 59, 60, 61], simulation of ballistic penetration [62, 63, 64, 65], and propagation of waves in inelastic geomechanics [66, 67, 68, 69, 70]. The above developments notwithstanding, the examination of plastic waves in variable cross-section media has received relatively little attention.

Recently, Dorgant *et al.* [71] examined plastic wave propagation in one-dimensional (1D) metamaterials composed of periodically-repeating unit cells.

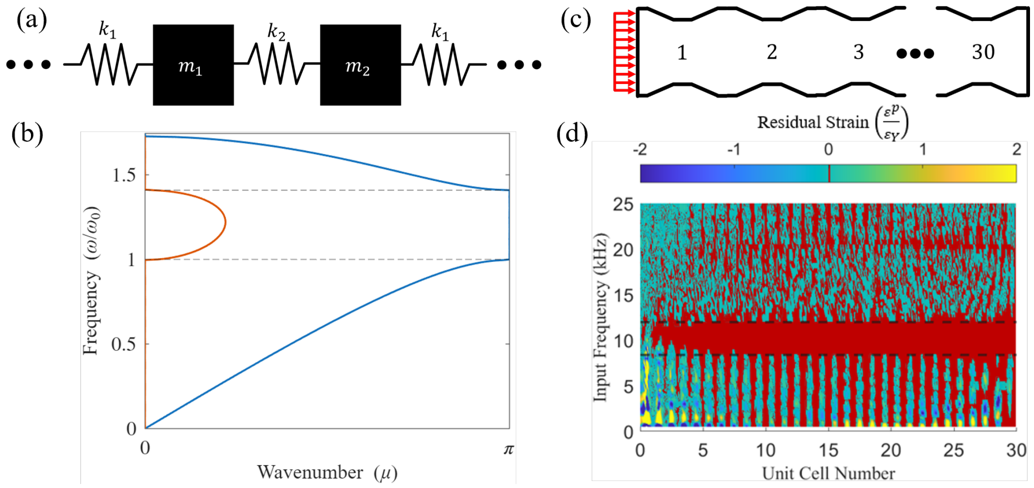

Figure 1: Linear diatomic mass-spring chain (a) and its band structure (b) with real (blue) and imaginary (orange) wavenumber components indicated. Frequencies within the bandgap (bounded by dashed lines) propagate as evanescent waves, decaying exponentially with distance. A continuous phononic crystal (c) composed of 30 unit cells and harmonically loaded beyond the elastic limit blocks elastic-plastic waves as evidenced in (d) where simulated residual strain (colorbar denotes magnitude) is plotted versus frequency and position (reproduced from [71]). Zero residual strain (absence of plasticity) appears red for emphasis while dashed lines indicate the elastic bandgap.

They applied the method of characteristics on a numerical space-time mesh for a 1D rod with a periodic cross-section (see Fig. 1(c)) subjected to amplitudes beyond the elastic limit. The medium studied featured a longitudinal, rate-independent constitutive relationship characterized by linear elastic and power-law plastic behavior with isotropic strain-hardening. The authors presented the residual strain surface versus frequency and position (reproduced in Fig. 1(d)) and, importantly, observed a bandgap effect on the plastic content, a result not previously reported.

In this paper, we design and fabricate a metamaterial system with hysteretic behavior analogous to the elastic-plastic constitutive laws studied in

[71], and then experimentally study plastic wave propagation as a function of frequency and amplitude. Specific focus is directed at the effect the bandgap has on elastic-plastic wave propagation. To do so, we first design a slider element containing a series stiffness (see Sec. 2.1) whose force-deflection curve features an elastic region followed by a slip region, producing hysteresis behavior analogous to that found in elastic-plastic constitutive laws. As such, the slip of the slider element serves as a surrogate for residual plastic strain. We then incorporate the slider element into a unit cell composed of two masses and multiple springs and form a diatomic chain (see Sec. 2.3) which we excite using an electrodynamic shaker (see Sec. 3). The diatomic chain serves as a discrete representation of a bi-sectional (or bi-material) metamaterial rod. At low amplitude excitation and in the absence of slip, the fabricated chain admits a response emulating elastic waves in the periodic rod, while at larger amplitudes sufficient to cause slip, the response mirrors elastic-plastic waves. Subsequently, we explore the effect that the system's bandgap has on the propagation of elastic-plastic waves. We conclude with remarks on suggested future research directions.

2. Component Design

2.1. Discrete Surrogate of Elastic-Plastic Constitutive Behavior

In designing a discrete surrogate for an elastic-plastic constitutive law, we draw inspiration from compliant slider (or Jenkins) elements, a historical representation of plasticity. Slider elements were first introduced in 1926 by

Masing [72, 73] to represent hysteretic plasticity and the cyclic strain hardening phenomenon known as the Bauschinger effect[1], and then by Prandtl [74] in 1928 to model metal plasticity by assuming a continuous distribution of compliant slider elements. Iwan [75, 76] later generalized these models by replacing a single slider with a continuum of such elements, each with a different yield force, allowing for a smooth hysteretic response closely matching known plastic material behavior.

Figure 2(a) illustrates a parallel Iwan model, while Fig. 2(b) depicts the model's force-deflection curve for a large number of slider elements, $n \gg 1$, with distributed strengths, $\phi_1 < \phi_2 < ... < \phi_n$. Under monotonic loading, each sliding component acts rigidly below a critical force level (stick) and slides above this force level (slip). As such, the slope of the force-deflection curve in Fig. 2(b) changes each time a slider element's critical force level is exceeded, corresponding to the slip of one sliding component. However, upon load reversal, all sliding components resume their stick states. Although many contemporary applications of slider elements and Iwan models typically focus on the dynamics of bolted joint interfaces [77, 78, 79], research concerning compliant slider elements as analogs to plasticity continues, commonly in the seismic literature [80, 81, 82].

We focus herein on a parallel Iwan model with only two slider elements,

---

[1] The Bauschinger effect describes the phenomenon whereby when a metal plastically deforms in one direction (e.g., in tension), the yield stress in the reverse direction (e.g., compression) reduces.

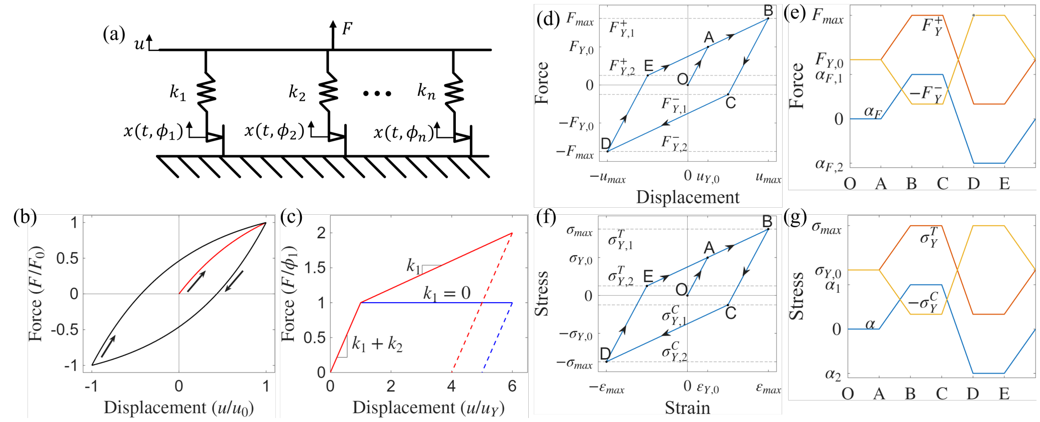

Figure 2: A parallel Iwan model (a) in which a system of n parallel slider elements are held rigidly on one side and displaced with force F on the other. The sliding component associated with the n^{th} slider element acts rigidly until the force it experiences exceeds its slider strength ϕ_n, after which the n^{th} slider element exhibits zero effective stiffness until load reversal. This behavior leads to the corresponding force-deflection graph (b) exhibiting hysteresis. Bi-linear force-deflection curves (c) realized from the parallel Iwan model using two slider elements (with $\phi_1 \to \infty$) yielding behavior analogous to an elastic-perfectly plastic constitutive relationship (blue) and an arbitrary bi-linear elastic-plastic constitutive relationship (red). For the loading path in (d), (e) depicts the evolution of the slip force (i.e., force to cause slip) in the positive (red) and negative (yellow) directions as well as their average (blue). For the loading path in (f), (g) depicts the evolution of the backstress (blue) and yield strengths in tension (red) and compression (yellow).

with stiffnesses denoted by k_1 and k_2 and strengths described by $\phi_1 \to \infty$ and ϕ_2. Figure 2(c) depicts two example force-deflection curves for this system: an elastic-perfectly plastic (blue) for a fully-compliant k_1 and a bi-linear elastic-plastic (red) for a finite value for k_1. The stick regime (elastic-analogous) includes forces up to the slip force $F_{Y,0}$ and has a slope of $k_1 + k_2$ while the slip regime (plastic-analogous) extends from $F_{Y,0}$ upward with a slope of k_1. For this two-slider element model, the applied force at which slip occurs, $F_{Y,0} = \frac{k_1+k_2}{k_2}\phi_2$, is analogous to the yield strength in the stress-strain relationship. Similarly, k_1+k_2 and k_1 are analogous to the stress-strain slopes in the elastic and plastic regimes, respectively.

Figures 2(d) and (e) display the force-displacement and slip force evolution, respectively, for the two-element parallel Iwan model. Under quasi-static, cyclic loading from rest at point O, the force reaches a maximum (F_{max}) at point B, and then a minimum ($-F_{max}$) at point D. Table 1 records the Iwan model's state – the applied force F, total displacement u, stretch in the second spring Δ_2, and second sliding component displacement s_2 – in terms of the spring stiffness values (k_1, k_2), the second slider strength (ϕ_2), and the maximum force (F_{max}) for each labeled point in Fig. 2(d). The Iwan model begins to slip at point A when the force on the second sliding component matches the slider strength, $F_A = F_{Y,0} = \phi_2 \frac{k_1+k_2}{k_2}$. After the second slider slips (between points A and B), only the first spring continues to deform. As the applied force begins to decrease (point B), the direction of displacement changes, causing the second sliding component to stick again. After this slider sticks, it next slips when the applied force on the sliding component is greater than the slider strength (at point C where the second spring is now in compression). Since the force at point B is greater than that at point A ($F_B - F_A = \Delta F$) and the slider strength remains constant for all time, the slip at C occurs at $F_C = -F_A + \Delta F$ such that $F_B - F_C = 2F_A$. From point C to point D, slip occurs in the negative direction and the sliding displacement s_2 decreases, effectively eliminating the plastic-like deformation accumulated from point A to B. After the applied force increases from point D, the sliding component locks again and the Iwan model displaces under the stick state. At point E, the force on the sliding component reaches its strength value and the model again slips in the positive direction. For symmetric loading ($F_B = |F_D|$), the path from E will align with the path from A to B, closing the hysteresis loop.

Parallel Iwan models exhibit force-deflection behavior analogous to kinematic strain hardening in which the yield in tension (or compression) reduces the yield strength in compression (or tension, respectively). Consider the hysteresis loop associated with a kinematic hardening, bi-linear stress-strain constitutive law depicted in Fig. 2(f) as well as the yield evolution depicted in Fig. 2(g) for the tensile yield σ_Y^T (orange), compressive yield σ_Y^C (yellow), and backstress $\alpha \equiv \sigma_Y^T + \sigma_Y^C$ (blue). The material is considered to undergo quasi-static, cyclic loading starting from rest at point O, reaching a maximum stress (σ_{max}) at point B, and then a minimum stress ($-\sigma_{max}$) at point D. As the stress evolves from point A to point B (loading in the plastic regime), the yield strength in tension increases to match the instantaneous stress, while the yield strength in compression decreases by a corresponding amount such that $\sigma_Y^T - \sigma_Y^C = 2\sigma_{Y,0}$ holds at every instant. When unloading occurs (from point B to point C), the material yields at a lower strength $|\sigma_Y^C| < \sigma_{Y,0}$. From point C to point D, compressive plastic deformation occurs, resulting in a decreased tensile yield strength and an increased compressive yield strength. As loading again increases in the tensile direction, the material yields at point E and plastically deforms, arriving back at point A. Table 2 summarizes the material state – the stress σ, total strain ε, elastic strain ε^e, and plastic strain

ε^p – in terms of the yield strength ($\sigma_{Y,0}$), elastic modulus (E), tangent modulus (or plastic stiffness, T), and maximum applied stress (σ_{max}) for each labeled point in Fig. 2(f). Kinematic hardening can be clearly mapped to the Iwan model by noting the similarity between the yield strength evolution in Fig. 2(g) with the slip force evolution in Fig. 2(e). Similarly, the back stress in Fig. 2(g) maps directly to the average sliding forces in Fig. 2(e).

Point	Force	Displacement	2^{nd} Spring Stretch	2^{nd} Slip Displacement
O	0	0	0	0
A	$F_{Y,0} \equiv \frac{k_1 + k_2}{k_2}\phi_2$	$\frac{\phi_2}{k_2}$	$\frac{\phi_2}{k_2}$	0
B	$F_{\max}$	$\frac{F_{\max} - \phi_2}{k_1}$	$\frac{\phi_2}{k_2}$	$\frac{F_{\max} - \phi_2}{k_1} - \frac{\phi_2}{k_2}$
C	$F_{\max} - 2\phi_2\frac{k_1 + k_2}{k_2}$	$\frac{F_{\max} - \phi_2}{k_1} - \frac{2\phi_2}{k_2}$	$-\frac{\phi_2}{k_2}$	$\frac{F_{\max} - \phi_2}{k_1} - \frac{\phi_2}{k_2}$
D	$-F_{\max}$	$-\frac{F_{\max} - \phi_2}{k_1}$	$-\frac{\phi_2}{k_2}$	$-\frac{F_{\max} - \phi_2}{k_1} + \frac{\phi_2}{k_2}$
E	$2\frac{k_1 + k_2}{k_2}\phi_2 - F_{\max}$	$-\frac{F_{\max} - \phi_2}{k_1} + \frac{2\phi_2}{k_2}$	$\frac{\phi_2}{k_2}$	$-\frac{F_{\max} - \phi_2}{k_1} + \frac{\phi_2}{k_2}$

Table 1: Iwan model's state at points A through E in Fig. 2(d) expressed in terms of the stiffness of each spring k_1, k_2, second slider strength ϕ_2, and the maximum applied force F_{max}.

2.2. Physical Realization of Iwan Model

We experimentally realize the sliding component of the chosen Iwan model using a support structure and a cylindrical sliding sleeve in frictional contact with follower elements, depicted as a CAD model and fabricated part in Figs. 3(a) and (b), respectively. An applied force of sufficient magnitude causes the steel sliding sleeve (green) to move relative to two followers (blue) and the support structure (shown transparent for illustrative purposes). Two

Point	Stress	Total Strain	Elastic Strain	Plastic Strain
O	0	0	0	0
A	$\sigma_{Y,0}$	$\frac{\sigma_{Y,0}}{E}$	$\frac{\sigma_{Y,0}}{E}$	0
B	$\sigma_{\max}$	$\frac{\sigma_{Y,0}}{E} + \frac{\sigma_{\max} - \sigma_{Y,0}}{T}$	$\frac{\sigma_{\max}}{E}$	$\frac{(\sigma_{\max} - \sigma_{Y,0})(E-T)}{ET}$
C	$\sigma_{\max} - 2\sigma_{Y,0}$	$-\frac{\sigma_{Y,0}}{E} + \frac{\sigma_{\max} - \sigma_{Y,0}}{T}$	$\frac{\sigma_{\max} - 2\sigma_{Y,0}}{E}$	$\frac{(\sigma_{\max} - \sigma_{Y,0})(E-T)}{ET}$
D	$-\sigma_{\max}$	$-\frac{\sigma_{Y,0}}{E} - \frac{\sigma_{\max} - \sigma_{Y,0}}{T}$	$-\frac{\sigma_{\max}}{E}$	$-\frac{(\sigma_{\max} - \sigma_{Y,0})(E-T)}{ET}$
E	$2\sigma_{Y,0} - \sigma_{\max}$	$\frac{\sigma_{Y,0}}{E} - \frac{\sigma_{\max} - \sigma_{Y,0}}{T}$	$\frac{2\sigma_{Y,0} - \sigma_{\max}}{E}$	$-\frac{(\sigma_{\max} - \sigma_{Y,0})(E-T)}{ET}$

Table 2: Material state at points A through E in Fig. 2(f) expressed in terms of the yield strength $\sigma_{Y,0}$, elastic modulus E, tangent or plastic modulus T, and the maximum applied stress $\sigma_{\max}$.

bolts generate a clamping pressure by altering the compression of the upper and lower helical springs, which in turn imposes a net normal force, F_N, on two followers whose clamping jaws are in direct contact with the cylindrical sliding sleeve. Furthermore, the springs and followers in the design enable a more precise modulation of F_N, effectively allowing for more turns of the bolts for a given normal force than would be possible with a simpler bolted connection. Thus, by adjusting the bolts' angular position, we can calibrate each sliding component's slip force. The frictional surfaces on both the sliding sleeve and the follower jaws are sanded to a smooth finish and lubricated with a multipurpose oil to both reduce wear on the surfaces as well as decrease the critical slip force. We fit this sliding component into a unit cell (see Sec. 2.3) using threaded through-holes in the sliding sleeve and the ends of the support structure.

Figure 3(c) depicts the experimental set-up for characterizing and tuning the sliding components. A frame secures the support structure while an electrodynamic shaker excites the sliding component from below. A force transducer between the shaker and the sliding sleeve records the applied force. Two laser Doppler vibrometers (LDV's) measure the velocity of the sliding sleeve and the follower jaws at locations marked by orange and purple indicators in Fig. 3(c). Hereafter, we denote the motion of the sliding sleeve relative to the followers as slip (i.e., slip displacement, velocity, acceleration). Figure 3(d) overlays the sleeve velocity (solid blue), follower velocity (dashed blue), and the applied force (red) for an example experimental data set. When the two velocity measurements align (negligible slip velocity), the sliding component is in a stick state; otherwise, it is considered to be in a slip state. Figure 3(e) depicts the slip and stick states together with the slip velocity (blue) and the measured force (red). We note from Fig. 3(e) that the stick regime features a slight non-zero slip velocity which arises from the small amount of compliance between the points of measurement on the sleeve and follower.

Each sliding component is calibrated by iteratively adjusting the bolts' angular position until slip occurs at a designated critical slip force (chosen to be ≈ 10 N). We determine the slip force for a given sliding component from the force and velocity measurements in Fig. 3(d) using the procedure graphically demonstrated for one slip event in Fig. 3(f). We find the instant of slip by first noting the time, t_i, at which the slip velocity, v_s, exceeds a set threshold, v_T, such that $|v_s(t_i)| > v_T > |v_s(t_{i-1})|$. Since this velocity threshold (chosen to be $v_T = 10$ mm/s) only approximates when slip occurs, we determine the slip force as the force measurement j time steps prior to the threshold crossing, $F_s = F(t_{i-j})$. Examining one slip event in one sliding component, we obtain the experimental constant j (chosen to be $j = 5$ resulting in $t_i - t_{i-j} \approx 0.5$ ms) such that the slip velocity begins to increase from the stuck state at t_{i-j}. The choice of j is confirmed by noting that the determined slip force is uniform for all slip events in the tested sliding component as well as across all slip events in each of the remaining sliding components.

2.3. Unit Cell Design & Verification

We design the unit cell first using a discrete representation, as depicted in Fig. 4(a), followed by a conceptual design, as illustrated by CAD models in Figs. 4(b)-(c). Steel disks (blue) having masses of approximately 0.95 kg and 1.25 kg are coupled via three outer helical springs (red) in parallel with the sliding component (green) and a center helical spring (purple). In relation to the parallel Iwan model introduced in Sec. 2.1, the three outer springs yield equivalent stiffness k_1, while the center spring and the sliding component yield k_2 and ϕ_2, respectively. Note that when the applied force exceeds the slip force, the stiffness changes from $4k$ to $3k$, where $k \approx 90.5$ kN/m, resulting in bi-linear force-deflection behavior.

To verify the mass and stiffness of each fabricated unit cell (without slider elements) and to assess any variability, we measure their frequency responses using the test set-up depicted in Fig. 4(d). An electrodynamic shaker excites the unit cell at the bottom using a frequency sweep, while a force transducer measures the excitation at the input (red indicator) and an LDV measures velocity at an output point (purple indicator). We then compute the mobility frequency response, an example of which appears in Fig. 4(e), by taking the ratio of peak velocity to force at each frequency input. The table appearing in Fig. 4(f) summarizes the obtained resonant peaks for each unit cell. From the chosen mass and stiffness values, we expect natural frequencies at approximately 47 and 134 Hz, which are in satisfactory agreement with the averaged measured resonant peaks of 45 and 138 Hz. More importantly, a low degree of disorder can be observed in the as-fabricated cells. Using the experimentally-obtained mass and stiffness values, and accounting for the added mass and stiffness of the slider elements, the expected band structure for the PnC, depicted in Fig. 4(g), predicts a frequency bandgap between 116 and 131 Hz. This bandgap guides interpretation of data obtained subsequently.

3. Phononic Crystal Experiment and Results

We construct the ten-cell PnC by freely hanging the unit cells from the top of a $3 \times 0.3 \times 0.3$ meter test frame as shown in Fig. 5(a). During assembly, the sliding components are secured only after all unit cells are hung, thereby mitigating the influence of gravity on the critical slip force. Without this precaution, sliding components located higher in the PnC would support the weight of the cells below, resulting in nonuniform preload and asymmetric slip behavior. Specifically, the lowest sliding component would remain centered on its slip surface, slipping symmetrically in tension and compression ($-F_Y^- = F_Y^+$), whereas the uppermost sliding component would slip more readily under downward loading ($-F_Y^- < F_Y^+$).

We first excite the PnC using an electrodynamic shaker at the bottom of the PnC with a 100 Hz Hanning-windowed harmonic signal. This frequency lies significantly outside the predicted bandgap and is selected to study plasticity effects absent from bandgap-induced attenuation. A force transducer and an LDV measure the input force and output velocity at the bottom and top of the PnC, respectively. Accelerometers on either side of the frictional interface of each sliding component capture the slip acceleration throughout the PnC, enabling spatial assessment of plastic response. Figure 5 illustrates the qualitative difference between elastic (b,d) and plastic (c,e) – corresponding to responses without and with slip, respectively – amplitude excitations by overlaying the follower (red) and sleeve (blue) acceleration (b,c) as well as the slip acceleration normalized against the maximum sleeve acceleration (d,e) at the sixth slider element away from the shaker (i.e., end of third unit cell). Under elastic amplitude excitation ($\approx$ 10 N), no slip occurs and the two accelerometer signals largely agree leading to a small normalized slip acceleration. Under plastic amplitude excitation ($\approx$ 50 N), the force on the sliding component exceeds the slip threshold, resulting in frequent slip events and a pronounced normalized slip acceleration (i.e., difference in the two acceleration signals). Although the slip acceleration is expected to be zero for the elastic case, Fig. 5(d) exhibits a small slip acceleration due to experimental factors such as instrument placement, divergence from rigid assumptions, etc., consistent with trends observed during individual slider testing (Sec. 2.2). In addition to the low normalized slip acceleration, the elastic excitation produces a slip acceleration of similar shape and frequqncy content to the excitation signal, indicating a linear system (few to no slip events). In contrast, the slip acceleration in response to plastic excitation undergoes a distinct change in behavior as the force increases beyond the critical level, reflecting an expected change in the governing system dynamics (slip-stick transitions) for the targeted nonlinear system.

We next excite the PnC in a frequency sweep between 105-135 Hz at elastic ($\approx$ 10 N) and plastic ($\approx$ 50 N) amplitudes to probe the effect of the bandgap (between 116-131 Hz) on elastic and elastic-plastic waves. Figure 6(a) overlays the normalized mobility at the last unit cell for elastic and plastic amplitude excitation with vertical dashed lines marking the predicted bandgap frequency bounds. Additionally, Fig. 6(b) plots the root-mean-square (RMS) slip accelerance – defined as the ratio between the RMS slip acceleration and the RMS force at each frequency – as a surface over frequency and slider position. Red lines denote the frequency bounds of the model-predicted bandgap. Analogous to Fig. 1(d), this surface visualizes the presence and strength of plasticity in the PnC across space and frequency.

Results presented in Fig. 6 provide clear evidence of a Bragg-scattering bandgap affecting both elastic and elastic-plastic waves. As shown in Fig. 6(a), elastic excitation produces a pronounced reduction in mobility within the predicted bandgap. More importantly, the plastic response exhibits a comparable attenuation over the same frequency range, consistent with earlier numerical observations [71] that frequency bandgaps impede elastic–plastic wave propagation. Figure 6(b) provides additional evidence of Bragg scattering in the elastic–plastic system through the spatial localization trend at the start of the PnC. For plastic excitation ($\approx$ 50 N) at frequencies within the bandgap, the slip accelerance is significantly elevated near the input end of the phononic crystal in comparison to later unit cells. As Bragg-scattering leads to internal reflections at the bandgap frequencies, the PnC traps and focuses energy in the first few unit cells, resulting in amplified slip acceleration. In contrast, frequencies outside the bandgap do not exhibit comparable spatial localization. While the observed attenuation of elastic-plastic waves in Fig. 6(a) and localization in Fig. 6(b) is likely due to Bragg scattering of the elastic precursor, the inability to invoke a superposition argument in the nonlinear setting makes an absolute determination of the mechanism difficult.

4. Concluding Remarks

This work measured elastic-plastic waves in a discrete phononic crystal whose force–deflection response is analogous to hysteretic elastic–plastic response. A discrete slider element was experimentally realized to introduce controllable plastic-analogous behavior at prescribed force levels. By incorporating this element into a linear unit-cell architecture, a modular phononic crystal was constructed, enabling validation of individual components prior to full assembly. Frequency-sweep experiments demonstrated clear bandgap behavior under both elastic and plastic excitation. Comparison of responses across excitation amplitudes confirmed the ability to achieve elastic- and plastic-analogous behavior at relatively low force levels (on the order of 10^1 N). Importantly, these results experimentally demonstrate that bandgaps attenuate elastic–plastic waves in a manner similar to linear elastic waves.

Recognizing that elastic metamaterial mechanisms remain effective in the plastic regime suggests new opportunities for applying these materials to elastic–plastic engineering problems. Future work may explore targeted applications of PnC concepts for use in vibration and damage mitigation, vehicle crashworthiness, and asset protection. Additional studies may also examine the limits of the present approach, including the role of bandgap phenomena under higher-amplitude loading conditions such as shock and hydrodynamic regimes.

Acknowledgments

Declarations

- Conflict of interest/Competing interests – The authors declare that they have no conflict of interest.
- Ethics approval – Not Applicable.

- Consent to participate – Not Applicable.

- Consent for publication – Not Applicable.

- Availability of data and materials – The data that support the findings of this study are available from the corresponding author, upon reasonable request.

- Authors' contributions – All authors contributed to the study conception and design. G.D. formulated the problem, conducted experimental testing, performed data analysis, and drafted the manuscript. M.J.L. conceived the experiment, supervised the experimental testing and data analysis, and drafted the manuscript. All authors read and approved the final manuscript.

References

[1] E. N. Economou and M. Sigalas. Stop bands for elastic waves in periodic composite materials. *The Journal of the Acoustical Society of America*, 95(4):1734–1740, 04 1994. ISSN 0001-4966. doi: 10.1121/1.408692. URL https://doi.org/10.1121/1.408692.

[2] Zhengyou Liu, Xixiang Zhang, Yiwei Mao, Y. Y. Zhu, Zhiyu Yang, C. T. Chan, and Ping Sheng. Locally resonant sonic materials. *Science*, 289(5485):1734–1736, 2000. doi: 10.1126/science.289.5485.1734. URL https://www.science.org/doi/abs/10.1126/science.289.5485.1734.

[3] Manvir S. Kushwaha. Stop-bands for periodic metallic rods: Sculptures that can filter the noise. *Applied Physics Letters*, 70(24):3218–3220, 06 1997. ISSN 0003-6951. doi: 10.1063/1.119130. URL https://doi.org/10.1063/1.119130.

[4] J. V. Sánchez-Pérez, D. Caballero, R. Mártinez-Sala, C. Rubio, J. Sánchez-Dehesa, F. Meseguer, J. Llinares, and F. Gálvez. Sound attenuation by a two-dimensional array of rigid cylinders. *Phys. Rev. Lett.*, 80:5325–5328, Jun 1998. doi: 10.1103/PhysRevLett.80.5325. URL https://link.aps.org/doi/10.1103/PhysRevLett.80.5325.

[5] D. Richards and D.J. Pines. Passive reduction of gear mesh vibration using a periodic drive shaft. *Journal of Sound and Vibration*, 264(2):317–342, 2003. ISSN 0022-460X. doi: https://doi.org/10.1016/S0022-460X(02)01213-0. URL https://www.sciencedirect.com/science/article/pii/S0022460X02012130.

[6] Z. Yang, H. M. Dai, N. H. Chan, G. C. Ma, and Ping Sheng. Acoustic metamaterial panels for sound attenuation in the 50–1000 hz regime. *Applied Physics Letters*, 96(4):041906, 01 2010. ISSN 0003-6951. doi: 10.1063/1.3299007. URL https://doi.org/10.1063/1.3299007.

[7] José Sánchez-Dehesa, Victor M. Garcia-Chocano, Daniel Torrent, Francisco Cervera, Suitberto Cabrera, and Francisco Simon. Noise control by sonic crystal barriers made of recycled materials. *The Journal of the*

Acoustical Society of America, 129(3):1173–1183, 03 2011. ISSN 0001-4966. doi: 10.1121/1.3531815. URL https://doi.org/10.1121/1.3531815.

[8] Anton Evgrafov, Cory J. Rupp, Martin L. Dunn, and Kurt Maute. Optimal synthesis of tunable elastic wave-guides. *Computer Methods in Applied Mechanics and Engineering*, 198(2):292–301, 2008. ISSN 0045-7825. doi: https://doi.org/10.1016/j.cma.2008.08.001. URL https://www.sciencedirect.com/science/article/pii/S0045782508002867.

[9] A. A. Maznev and V. E. Gusev. Waveguiding by a locally resonant metasurface. *Phys. Rev. B*, 92:115422, Sep 2015. doi: 10.1103/PhysRevB.92.115422. URL https://link.aps.org/doi/10.1103/PhysRevB.92.115422.

[10] Liang-Yu Wu, Lien-Wen Chen, and Chia-Ming Liu. Acoustic energy harvesting using resonant cavity of a sonic crystal. *Applied Physics Letters*, 95(1):013506, 07 2009. ISSN 0003-6951. doi: 10.1063/1.3176019. URL https://doi.org/10.1063/1.3176019.

[11] Stefano Gonella, Albert C. To, and Wing Kam Liu. Interplay between phononic bandgaps and piezoelectric microstructures for energy harvesting. *Journal of the Mechanics and Physics of Solids*, 57(3):621–633, 2009. ISSN 0022-5096. doi: https://doi.org/10.1016/j.jmps.2008.11.002. URL https://www.sciencedirect.com/science/article/pii/S0022509608001919.

[12] M Carrara, M R Cacan, J Toussaint, M J Leamy, M Ruzzene, and

A Erturk. Metamaterial-inspired structures and concepts for elastoacoustic wave energy harvesting. *Smart Materials and Structures*, 22 (6):065004, apr 2013. doi: 10.1088/0964-1726/22/6/065004. URL https://doi.org/10.1088/0964-1726/22/6/065004.

[13] Xiangdong Zhang and Zhengyou Liu. Negative refraction of acoustic waves in two-dimensional phononic crystals. *Applied Physics Letters*, 85 (2):341–343, 07 2004. ISSN 0003-6951. doi: 10.1063/1.1772854. URL https://doi.org/10.1063/1.1772854.

[14] Lezheng Fang and Michael J. Leamy. Negative refraction in mechanical rotator lattices. *Phys. Rev. Appl.*, 18:064058, Dec 2022. doi: 10.1103/PhysRevApplied.18.064058. URL https://link.aps.org/doi/10.1103/PhysRevApplied.18.064058.

[15] Bogdan-Ioan Popa, Lucian Zigoneanu, and Steven A. Cummer. Experimental acoustic ground cloak in air. *Phys. Rev. Lett.*, 106:253901, Jun 2011. doi: 10.1103/PhysRevLett.106.253901. URL https://link.aps.org/doi/10.1103/PhysRevLett.106.253901.

[16] Shu Zhang, Chunguang Xia, and Nicholas Fang. Broadband acoustic cloak for ultrasound waves. *Phys. Rev. Lett.*, 106:024301, Jan 2011. doi: 10.1103/PhysRevLett.106.024301. URL https://link.aps.org/doi/10.1103/PhysRevLett.106.024301.

[17] Steven A Cummer and David Schurig. One path to acoustic cloaking.

New Journal of Physics, 9(3):45, mar 2007. doi: 10.1088/1367-2630/9/3/045. URL https://doi.org/10.1088/1367-2630/9/3/045.

[18] Y. Pennec, B. Djafari-Rouhani, J. O. Vasseur, A. Khelif, and P. A. Deymier. Tunable filtering and demultiplexing in phononic crystals with hollow cylinders. *Phys. Rev. E*, 69:046608, Apr 2004. doi: 10.1103/PhysRevE.69.046608. URL https://link.aps.org/doi/10.1103/PhysRevE.69.046608.

[19] Haoyi Cheng, Jingwen Guo, Xin Zhang, and Wenjing Ye. Frequency-multiplexed transmitted-wave manipulation with multifunctional acoustic metasurfaces. *Phys. Rev. Appl.*, 20:034009, Sep 2023. doi: 10.1103/PhysRevApplied.20.034009. URL https://link.aps.org/doi/10.1103/PhysRevApplied.20.034009.

[20] G. Chakraborty and A.K. Mallik. Dynamics of a weakly non-linear periodic chain. *International Journal of Non-Linear Mechanics*, 36(2):375–389, 2001. ISSN 0020-7462. doi: https://doi.org/10.1016/S0020-7462(00)00024-X. URL https://www.sciencedirect.com/science/article/pii/S002074620000024X.

[21] K. Bertoldi and M. C. Boyce. Wave propagation and instabilities in monolithic and periodically structured elastomeric materials undergoing large deformations. *Phys. Rev. B*, 78:184107, Nov 2008. doi: 10.1103/PhysRevB.78.184107. URL https://link.aps.org/doi/10.1103/PhysRevB.78.184107.

[22] Raj K. Narisetti, Massimo Ruzzene, and Michael J. Leamy. Study of wave propagation in strongly nonlinear periodic lattices using a harmonic balance approach. *Wave Motion*, 49(2):394–410, 2012. ISSN 0165-2125. doi: https://doi.org/10.1016/j.wavemoti.2011.12.005. URL https://www.sciencedirect.com/science/article/pii/S0165212511001478.

[23] C Daraio, V.F. Nesterenko, E.B. Herbold, and S. Jin. Tunability of solitary wave properties in one-dimensional strongly nonlinear phononic crystals. *Physical Review E*, 73:026610, 2006. doi: 10.1103/PhysRevE.73.026610. URL https://doi.org/10.1103/PhysRevE.73.026610.

[24] Neel Nadkarni, Chiara Daraio, and Dennis M. Kochmann. Dynamics of periodic mechanical structures containing bistable elastic elements: From elastic to solitary wave propagation. *Phys. Rev. E*, 90:023204, Aug 2014. doi: 10.1103/PhysRevE.90.023204. URL https://link.aps.org/doi/10.1103/PhysRevE.90.023204.

[25] B. Deng, J. R. Raney, K. Bertoldi, and V. Tournat. Nonlinear waves in flexible mechanical metamaterials. *Journal of Applied Physics*, 130(4):040901, 07 2021. ISSN 0021-8979. doi: 10.1063/5.0050271. URL https://doi.org/10.1063/5.0050271.

[26] N. Boechler, G. Theocharis, and C. Daraio. Bifurcation-based acoustic switching and rectification. *Nature Mater*, 10:665–668, 2011. doi: 10.1038/nmat3072.

[27] BI. Popa and S. Cummer. Non-reciprocal and highly nonlinear active acoustic metamaterials. *Nat Commun*, 5:3398, 2014. doi: 10.1038/ncomms4398.

[28] Keegan J Moore, Jonathan Bunyan, Sameh Tawfick, Oleg V Gendelman, Shuangbao Li, Michael Leamy, and Alexander F Vakakis. Nonreciprocity in the dynamics of coupled oscillators with nonlinearity, asymmetry, and scale hierarchy. *Physical Review E*, 97(1):012219, 2018.

[29] Matthew D Fronk, Sameh Tawfick, Chiara Daraio, Shuangbao Li, Alexander Vakakis, and Michael J Leamy. Acoustic non-reciprocity in lattices with nonlinearity, internal hierarchy, and asymmetry: Computational study. *Journal of vibration and acoustics*, 141(5):051011, 2019.

[30] Lezheng Fang, Alireza Mojahed, Amir Darabi, Alexander F Vakakis, and Michael J Leamy. Passive nonreciprocity in a system of asymmetrical rotational oscillators. *Physical Review Applied*, 15(3):034005, 2021.

[31] Z. Li, Y. Wang, and Y. Wang. Tunable three-dimensional nonreciprocal transmission in a layered nonlinear elastic wave metamaterial by initial stresses. *Appl. Math. Mech.-Engl.*, 43:167–184, 2022. doi: 10.1007/s10483-021-2808-9.

[32] Jordan R. Raney, Neel Nadkarni, Chiara Daraio, Dennis M. Kochmann, Jennifer A. Lewis, and Katia Bertoldi. Stable propagation of mechanical signals in soft media using stored elastic energy. *Proceed-*

ings of the National Academy of Sciences, 113(35):9722–9727, 2016. doi: 10.1073/pnas.1604838113. URL https://www.pnas.org/doi/abs/10.1073/pnas.1604838113.

[33] F. Li, P. Anzel, and J. et al. Yang. Granular acoustic switches and logic elements. *Nat Commun*, 5(5311), 2014. doi: 10.1038/ncomms6311.

[34] Kevin L. Manktelow, Michael J. Leamy, and Massimo Ruzzene. Weakly nonlinear wave interactions in multi-degree of freedom periodic structures. *Wave Motion*, 51(6):886–904, 2014. ISSN 0165-2125. doi: https://doi.org/10.1016/j.wavemoti.2014.03.003. URL https://www.sciencedirect.com/science/article/pii/S0165212514000390.

[35] Alessandro Spadoni and Chiara Daraio. Generation and control of sound bullets with a nonlinear acoustic lens. *Proceedings of the National Academy of Sciences*, 107(16):7230–7234, 2010. doi: 10.1073/pnas.1001514107. URL https://www.pnas.org/doi/abs/10.1073/pnas.1001514107.

[36] Nehemiah Mork, Matthew D. Fronk, Laura B. Biedermann, Michael B. Sinclair, and Michael J. Leamy. Hierarchical unit cell employing a nonlinear energy sink for passive, low-pass amplitude filtering of acoustic waves. *Extreme Mechanics Letters*, 63:102056, 2023. ISSN 2352-4316. doi: https://doi.org/10.1016/j.eml.2023.102056. URL https://www.sciencedirect.com/science/article/pii/S2352431623001025.

[37] Jinkyu Yang, Claudio Silvestro, Sophia N Sangiorgio, Sean L Borkowski, Edward Ebramzadeh, Luigi De Nardo, and Chiara Daraio. Nondestructive evaluation of orthopaedic implant stability in tha using highly nonlinear solitary waves. *Smart Materials and Structures*, 21 (1):012002, dec 2011. doi: 10.1088/0964-1726/21/1/012002. URL https://doi.org/10.1088/0964-1726/21/1/012002.

[38] R. Khajehtourian and M. I. Hussein. Dispersion characteristics of a nonlinear elastic metamaterial. *AIP Advances*, 4(12):124308, 12 2014. ISSN 2158-3226. doi: 10.1063/1.4905051. URL https://doi.org/10.1063/1.4905051.

[39] H. Reda, N. Karathanasopoulos, J.F. Ganghoffer, and H. Lakiss. Wave propagation characteristics of periodic structures accounting for the effect of their higher order inner material kinematics. *Journal of Sound and Vibration*, 431:265–275, 2018. ISSN 0022-460X. doi: https://doi.org/10.1016/j.jsv.2018.06.006. URL https://www.sciencedirect.com/science/article/pii/S0022460X18303602.

[40] Matthew D Fronk, Lezheng Fang, Pawel Packo, and Michael J Leamy. Elastic wave propagation in weakly nonlinear media and metamaterials: a review of recent developments. *Nonlinear Dynamics*, 111(12):10709–10741, 2023.

[41] H. Kolsky and L.S. Douch. Experimental studies in plastic wave propagation. *Journal of the Mechanics and Physics of Solids*, 10

(3):195–223, 1962. ISSN 0022-5096. doi: https://doi.org/10.1016/0022-5096(62)90038-8. URL https://www.sciencedirect.com/science/article/pii/0022509662900388.

[42] LH Donnell. Longitudinal wave transmission and impact. *Trans. ASME*, 52, 1930.

[43] G.I. Taylor. The use of flat-ended projectiles for determining dynamic yield stress i. theoretical considerations. *Proceedings of the Royal Society of London. Series A. Mathematical and Physical Sciences*, 194:289–299, 1948.

[44] Theodore Von Karman and Pol Duwez. The propagation of plastic deformation in solids. *Journal of Applied Physics*, 21, 1950.

[45] M.P. White and L. Griffis. The propagation of plasticity in uniaxial compression. *ASME. J. Appl. Mech.*, 15(3), 1948.

[46] Kh. A. Rakhmatulin. On propagation of unloading waves. *Prikl. Mat. Mekh.*, 9, 1945.

[47] Kh A Rakhmatulin and GS Shapiro. On the propagation of plane elastic-plastic waves. *Appl. Mech. Math*, 12:369–374, 1948.

[48] GS Shapiro. Longitudinal vibrations of a rod. *Prikl. Mat. Meh.*, 10: 597–616, 1946.

[49] L. E. Malvern. Plastic wave propagation in a bar of material exhibiting a strain rate effect. *Quarterly of Applied Mathematics*, 8, 1951.

[50] Piotr Perzyna. Fundamental problems in viscoplasticity. In G.G. Chernyi, H.L. Dryden, P. Germain, L. Howarth, W. Olszak, W. Prager, R.F. Probstein, and H. Ziegler, editors, *Advances in Applied Mechanics*, volume 9, pages 243–377. Elsevier, 1966. doi: https://doi.org/10.1016/S0065-2156(08)70009-7. URL https://www.sciencedirect.com/science/article/pii/S0065215608700097.

[51] Tatsuo Tokuoka. Acceleration waves in rate type plastic material with general work-hardening. *International Journal of Non-Linear Mechanics*, 13(4):199–204, 1978. ISSN 0020-7462. doi: https://doi.org/10.1016/0020-7462(78)90022-7. URL https://www.sciencedirect.com/science/article/pii/0020746278900227.

[52] E. H. Lee and D. T. Liu. Finite-strain elastic—plastic theory with application to plane-wave analysis. *Journal of Applied Physics*, 38 (1):19–27, 01 1967. ISSN 0021-8979. doi: 10.1063/1.1708953. URL https://doi.org/10.1063/1.1708953.

[53] R.M. Brannon, W.J. Drugan, and Y. Shen. Requirements of thermodynamics in the analysis of elastic-plastic shock waves. *Journal of the Mechanics and Physics of Solids*, 43(6):973–1001, 1995. ISSN 0022-5096. doi: https://doi.org/10.1016/0022-5096(95)00009-8. URL https://www.sciencedirect.com/science/article/pii/0022509695000098.

[54] Bryan W. Reed, James S. Stolken, Roger W. Minich, and Mukul Kumar. A unified approach for extracting strength information from nonsimple compression waves. part i: Thermodynamics and numerical implementation. *Journal of Applied Physics*, 110(11):113505, 2011. doi: 10.1063/1.3653821. URL https://doi.org/10.1063/1.3653821.

[55] Dennis E. Grady. Microstructural effects on wave propagation in solids. *International Journal of Engineering Science*, 22(8): 1181–1186, 1984. ISSN 0020-7225. doi: https://doi.org/10.1016/0020-7225(84)90120-4. URL https://www.sciencedirect.com/science/article/pii/0020722584901204.

[56] R. Dingreville, J. Robbins, and T.E. Voth. Wave propagation and dispersion in elasto-plastic microstructured materials. *International Journal of Solids and Structures*, 51(11-12), 2014.

[57] S. K. Tomar and Suraj Kumar. Wave propagation in elastic–plastic material with voids. *Journal of Applied Physics*, 127(5):054901, 02 2020. ISSN 0021-8979. doi: 10.1063/1.5127903. URL https://doi.org/10.1063/1.5127903.

[58] H Kolsky. An investigation of the mechanical properties of materials at very high rates of loading. *Proceedings of the Physical Society. Section B*, 62(11):676–700, nov 1949. doi: 10.1088/0370-1301/62/11/302. URL https://dx.doi.org/10.1088/0370-1301/62/11/302.

[59] Jr. Foster, J. C., P. J. Maudlin, and S. E. Jones. On the taylor test: A continuum analysis of plastic wave propagation. *AIP Conference Proceedings*, 370(1):291–294, 05 1996. ISSN 0094-243X. doi: 10.1063/1.50710. URL https://doi.org/10.1063/1.50710.

[60] S.E. Jones, Paul J. Maudlin, and Joseph C. Foster. An engineering analysis of plastic wave propagation in the taylor test. *International Journal of Impact Engineering*, 19(2):95–106, 1997. ISSN 0734-743X. doi: https://doi.org/10.1016/S0734-743X(96)00020-6. URL https://www.sciencedirect.com/science/article/pii/S0734743X96000206.

[61] J. R. Asay, D. L. Hicks, and D. B. Holdridge. Comparison of experimental and calculated elastic-plastic wave profiles in lif. *Journal of Applied Physics*, 46(10):4316–4322, 10 1975. ISSN 0021-8979. doi: 10.1063/1.321454. URL https://doi.org/10.1063/1.321454.

[62] Charles E. Anderson and Sol R. Bodner. Ballistic impact: The status of analytical and numerical modeling. *International Journal of Impact Engineering*, 7(1):9–35, 1988. ISSN 0734-743X. doi: https://doi.org/10.1016/0734-743X(88)90010-3. URL https://www.sciencedirect.com/science/article/pii/0734743X88900103.

[63] Marco Di Sciuva, Carlo Frola, and Sergio Salvano. Low and high velocity impact on inconel 718 casting plates: ballistic limit and numerical correlation. *International Journal of Impact Engineering*, 28

(8):849–876, 2003. ISSN 0734-743X. doi: https://doi.org/10.1016/S0734-743X(02)00156-2. URL https://www.sciencedirect.com/science/article/pii/S0734743X02001562.

[64] M. Mamivand and G.H. Liaghat. A model for ballistic impact on multi-layer fabric targets. *International Journal of Impact Engineering*, 37 (7):806–812, 2010. ISSN 0734-743X. doi: https://doi.org/10.1016/j.ijimpeng.2010.01.003. URL https://www.sciencedirect.com/science/article/pii/S0734743X10000126.

[65] Srinivasan S. Naarayan and Ghatu Subhash. Wave propagation in ballistic gelatine. *Journal of the Mechanical Behavior of Biomedical Materials*, 68:32–41, 2017. ISSN 1751-6161. doi: https://doi.org/10.1016/j.jmbbm.2017.01.030. URL https://www.sciencedirect.com/science/article/pii/S1751616117300383.

[66] W. Heierli. Inelastic wave propagation in soil columns. *Journal of the Soil Mechanics and Foundations Division*, 88(6):33–63, 1962. doi: 10.1061/JSFEAQ.0000476. URL https://ascelibrary.org/doi/abs/10.1061/JSFEAQ.0000476.

[67] *Pulse Propagation In Rocks*, volume All Days of *U.S. Rock Mechanics/Geomechanics Symposium*, 09 1966.

[68] Fabrice Dupros, Florent De Martin, Evelyne Foerster, Dimitri Komatitsch, and Jean Roman. High-performance finite-element simulations

of seismic wave propagation in three-dimensional nonlinear inelastic geological media. *Parallel Computing*, 36(5):308–325, 2010. ISSN 0167-8191. doi: https://doi.org/10.1016/j.parco.2009.12.011. URL https://www.sciencedirect.com/science/article/pii/S0167819109001331. Parallel Matrix Algorithms and Applications.

[69] Abbas Haider, Erxiang Song, and Peng Li. Numerical simulation and absorbing boundary conditions for wave propagation in a semi-infinite media with a linear isotropic hardening plastic model. *Soil Dynamics and Earthquake Engineering*, 125:105627, 2019. ISSN 0267-7261. doi: https://doi.org/10.1016/j.soildyn.2019.04.001. URL https://www.sciencedirect.com/science/article/pii/S0267726118307139.

[70] L. Lang, K.I. Song, Y. Zhai, D. Lao, and H.L. Lee. Stress wave propagation in viscoelastic-plastic rock-like materials. *Materials*, 9 (5), 2016. ISSN 1996-1944. doi: 10.3390/ma9050377. URL https://www.mdpi.com/1996-1944/9/5/377.

[71] G. Dorgant, W. DeLima, and M.J. Leamy. Elastic–plastic wave propagation in phononic crystals. *Nonlinear Dynamics*, 113:23815—23838, 2025. doi: 10.1007/s11071-024-10665-0. URL https://doi.org/10.1007/s11071-024-10665-0.

[72] G. Masing. Internal stresses and work hardening in brass. In *Proceedings of Second International Congress of Applied Mechanics*, pages 332–335, Zurich, 1926.

[73] *Iwan Models and Their Provenance*, volume Volume 1: 24th Conference on Mechanical Vibration and Noise, Parts A and B of *International Design Engineering Technical Conferences and Computers and Information in Engineering Conference*, 08 2012. doi: 10.1115/DETC2012-71534. URL https://doi.org/10.1115/DETC2012-71534.

[74] L. Prandtl. A conceptual model for the kinetic theory of solid bodies. *ZAMM - Journal of Applied Mathematics and Mechanics / Zeitschrift für Angewandte Mathematik und Mechanik*, 8(2):85–106, 1928. doi: https://doi.org/10.1002/zamm.19280080202. URL https://onlinelibrary.wiley.com/doi/abs/10.1002/zamm.19280080202.

[75] W. D. Iwan. A Distributed-Element Model for Hysteresis and Its Steady-State Dynamic Response. *Journal of Applied Mechanics*, 33(4):893–900, 12 1966. ISSN 0021-8936. doi: 10.1115/1.3625199. URL https://doi.org/10.1115/1.3625199.

[76] W. D. Iwan. On a Class of Models for the Yielding Behavior of Continuous and Composite Systems. *Journal of Applied Mechanics*, 34(3): 612–617, 09 1967. ISSN 0021-8936. doi: 10.1115/1.3607751. URL https://doi.org/10.1115/1.3607751.

[77] DANIEL J SEGALMAN. An initial overview of iwan modeling for mechanical joints. Technical report, Sandia National Labs., Albuquerque, NM (US); Sandia National Labs., Livermore, CA (US), 02 2001. URL https://www.osti.gov/biblio/780307.

[78] Ivan I. Argatov and Eric A. Butcher. On the iwan models for lap-type bolted joints. *International Journal of Non-Linear Mechanics*, 46 (2):347–356, 2011. ISSN 0020-7462. doi: https://doi.org/10.1016/j.ijnonlinmec.2010.09.018. URL https://www.sciencedirect.com/science/article/pii/S0020746210001514.

[79] M.R.W. Brake. A reduced iwan model that includes pinning for bolted joint mechanics. *Nonlinear Dyn*, 87:1335–1349, 2016. doi: https://doi.org/10.1007/s11071-016-3117-2.

[80] Jin-Sun Lee, Yun-Wook Choo, and Dong-Soo Kim. A modified parallel iwan model for cyclic hardening behavior of sand. *Soil Dynamics and Earthquake Engineering*, 29(4):630–640, 2009. ISSN 0267-7261. doi: https://doi.org/10.1016/j.soildyn.2008.06.008. URL https://www.sciencedirect.com/science/article/pii/S026772610800122X.

[81] S Chabot, E D Mercerat, N Glinsky, and L F Bonilla. An efficient algorithm for sampling the shear-modulus reduction curve in the context of wave propagation using the elastoplastic iwan model. *Geophysical Journal International*, 228(3):1907–1917, 10 2021. ISSN 0956-540X. doi: 10.1093/gji/ggab431. URL https://doi.org/10.1093/gji/ggab431.

[82] S.A. Whyte, H.J. Burd, C.M. Martin, and M.J. Rattley. Formulation and implementation of a practical multi-surface soil plasticity model. *Computers and Geotechnics*, 117:103092, 2020. ISSN 0266-

352X. doi: https://doi.org/10.1016/j.compgeo.2019.05.007. URL https://www.sciencedirect.com/science/article/pii/S0266352X1930148X.

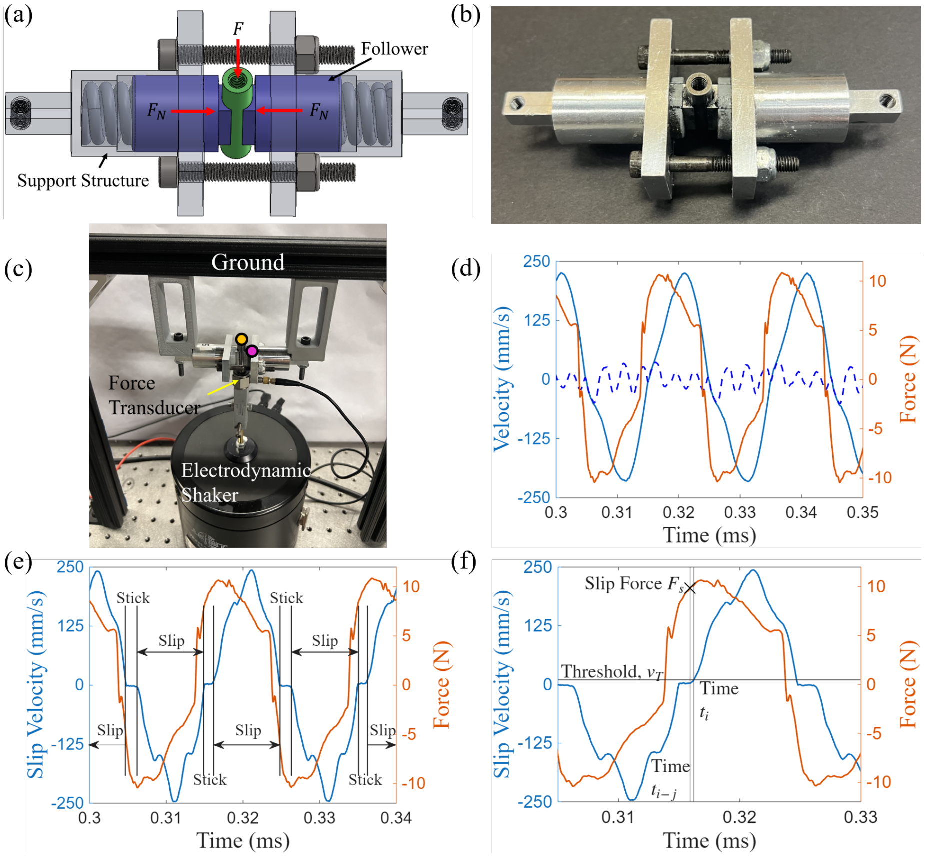

Figure 3: CAD model of the sliding component (a) and its as-fabricated realization (b) in which the sleeve (green) slides relative to the followers (blue) when the applied force exceeds a critical slip force. Each sliding component is calibrated with the experimental testing set-up (c) in which the input force is measured by a force transducer and the velocity at the sleeve and follower structure are measured with laser Doppler vibrometers at the yellow and pink indicators, respectively. An example data set (d) where the measured velocities of the sleeve (solid blue) and the follower (dashed blue) and the measured force (orange) correspond to the vertical axis of the same color; (e) demonstrates the slip and stick states with the slip velocity (blue) and force (orange), while (f) illustrates the slip force determination for a single slip event.

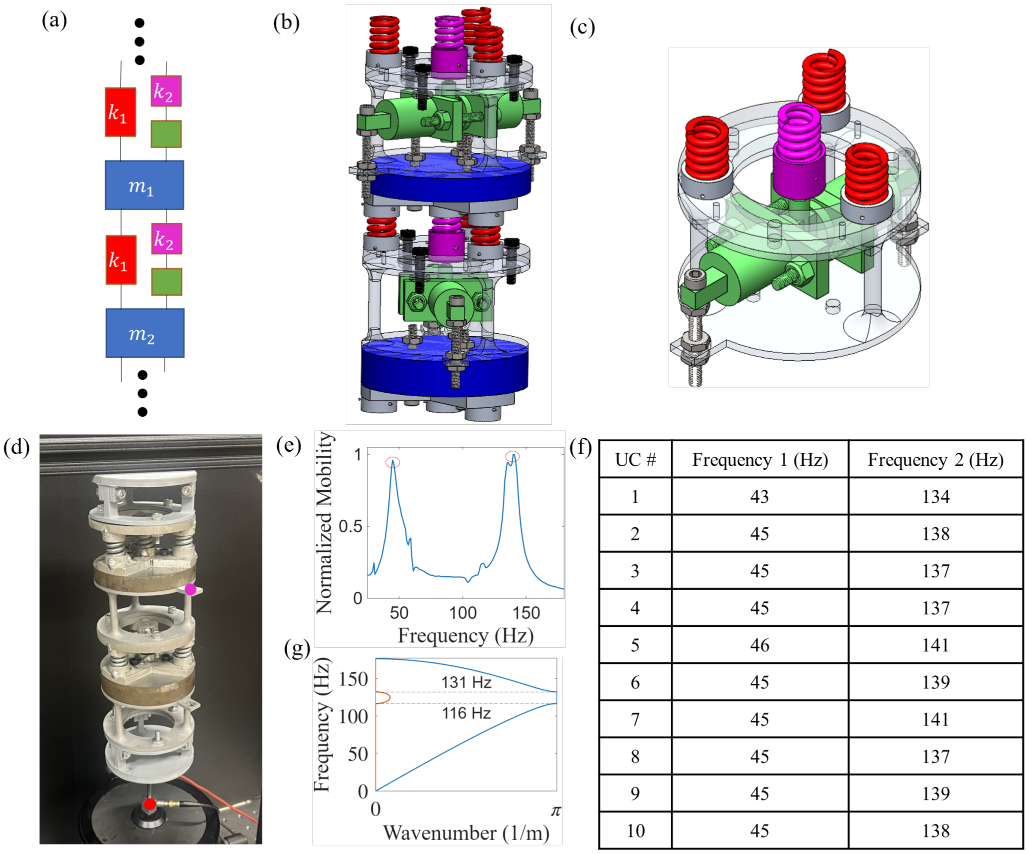

UC #	Frequency 1 (Hz)	Frequency 2 (Hz)
1	43	134
2	45	138
3	45	137
4	45	137
5	46	141
6	45	139
7	45	141
8	45	137
9	45	139
10	45	138

Figure 4: Discrete element depiction of the unit cell (a) and CAD model representation (b). An exploded view (c) of the slider element depicting the stiffness and sliding components in greater detail. The linear unit cell (b) – without the sliding component – is excited within the test set-up (d) for which the force input and unit cell response are measured by a force transducer and an LDV at the red and pink indicators, respectively. From these measurements, the (e) normalized mobility frequency response for each unit cell is obtained (an example unit cell measurement shown). The obtained frequency peaks of each unit cell, tabulated in (f), then inform the average unit cell mass and stiffness values from which is calculated the (g) linear elastic band structure. This band structure exhibits a bandgap between 116 and 131 Hz, bounded by the dashed lines, as evidenced by the nonzero imaginary part (orange) and the π or 0 real part (blue) of the wavenumber.

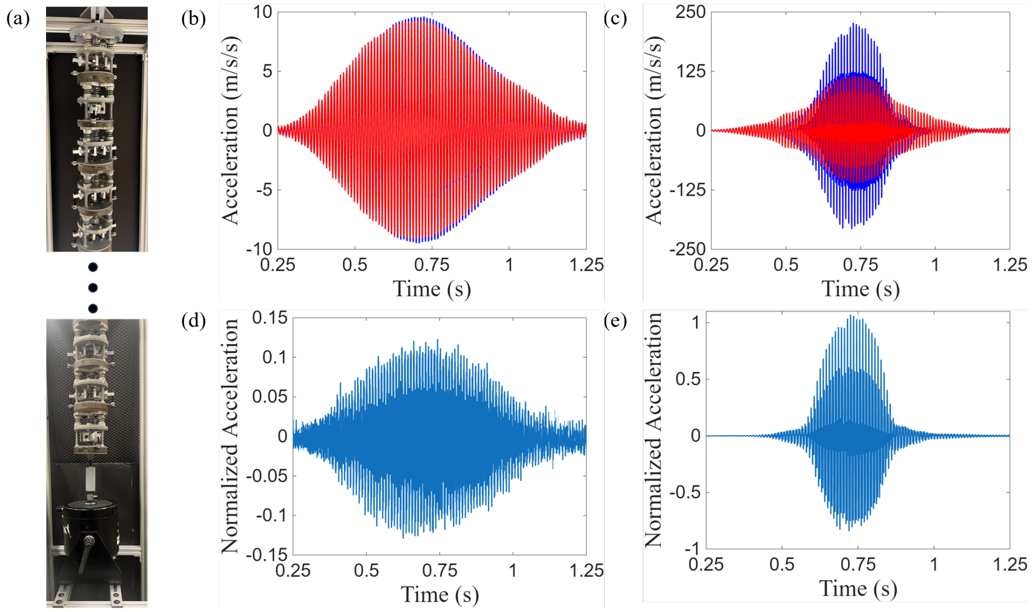

Figure 5: Example measurements at 100 Hz obtained from the set-up depicted in (a) for which the columns correspond to elastic (left) and plastic excitation (right) and the rows correspond to follower (red) and sleeve (blue) acceleration signals (top) and the slip acceleration (bottom), normalized to the maximum acceleration of the sleeve.

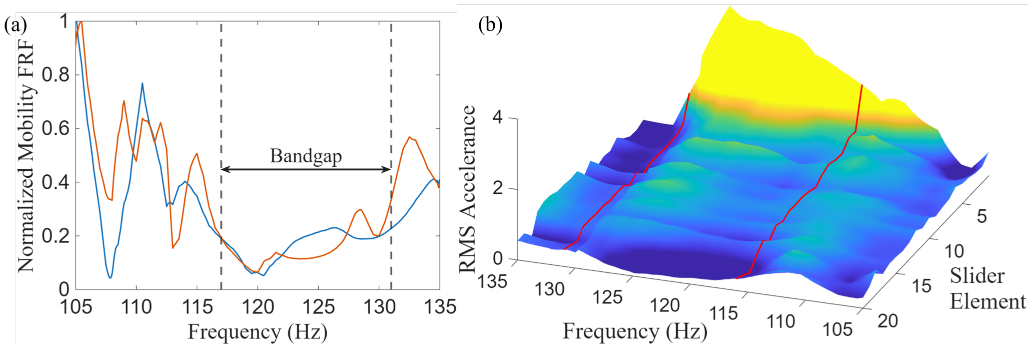

Figure 6: (a) Mobility frequency response, normalized to their respective maxima, for elastic (blue) and plastic (orange) amplitude excitation. Vertical dashed lines indicate the predicted bandgap. (b) Surface plot of the root-mean-square (RMS) slip accelerance (ratio between the RMS slip acceleration and the RMS force) at each sliding component as a function of frequency for plastic excitation (≈ 50 N). Red lines mark the edges of the predicted bandgap.